ADVANCED FUNCTIONAL MATERIALS
www.afm-journal.de

Electro-Active Polymer Actuated Microfiltration Membranes: Design, Performance, and Particle Dynamics

*Irem Gurbuz, Hanieh Bazyar, and Andres Hunt**

Membranes used in water treatment are prone to fouling, leading to flux decline, increased operational costs, and reduced lifespan. Conventional antifouling methods, such as chemical cleaning and backwashing, are effective but have significant drawbacks. This study introduces active polymeric microfiltration membranes with embedded self-cleaning functionality by printing electro-active polymer (EAP) actuators on porous PVDF and PTFE membranes. The design parameters for the membrane-actuators, including membrane material selection, actuator placement, and active layer thickness are investigated. During membrane excitation, resonance frequencies/modes, surface displacements, velocities, and accelerations are detected with laser Doppler vibrometer (PSV-400). By leveraging the electrostrictive properties of the P(VDF–TrFE–CTFE) terpolymer, the actuators generate out-of-plane surface vibrations, achieving average surface accelerations of up to 75 m s^{-2} (600 V, 4548 Hz) and local surface accelerations up to 255 m s^{-2} (600 V, 6560 Hz). Particle manipulation in air and aqueous media is respectively tested with randomly distributed metal alloy balls (200 µm diameter) and Iriodin 153 Flash Pearl suspension (1 wt%) on the active membranes. The dry metal alloy balls show strong resonant dislocations near 3500 Hz and 6700 Hz frequencies, while Iriodin 153 Flash Pearl particles (20–100 µm diameter) are visibly mobilized and redistributed at ≈3100 and 5400 Hz frequencies. The results indicate that mechanical agitation of filtration membranes via embedded actuation is a viable method for foulant mobilization, and will be further investigated for fouling mitigation in membrane filtration technologies.

1. Introduction

Membrane-based wastewater treatment supports environmental sustainability, and must align with Sustainable Development Goal 6 (SDG6) through affordable and eco-friendly technologies, which remain limited yet.[1] Developed countries have advanced systems but face aging infrastructure, environmental changes, and new contaminants, while developing countries grapple with fundamental water access and sanitation challenges.[2] The limitations and inefficiency of current wastewater treatment methods such as adsorption, bioremediation and hybrid approaches are the major contributors to water pollution[3] since inadequately treated industrial effluents are released into rivers, exacerbating the declining quality and quantity of groundwater and severely impacting the supply of safe drinking/domestic water.[4]

Over the past few decades, membrane technology has advanced considerably, driven by its potential advantages in water and wastewater treatment. These include the ability to reduce equipment footprint, enhance process efficiency, and lower energy and capital requirements under optimized conditions.[5] However, despite these promising features, membrane technologies still face significant barriers to widespread, large-scale implementation. These challenges include substantial energy demands in certain configurations, relatively high capital and operational costs, environmental concerns related to membrane disposal and chemical use, as well as membrane fouling.[6,7]

Membrane fouling occurs when solutes and particles accumulate on the membrane surface or clog its pores, increasing resistance within the membrane and reducing permeation.[7] This significantly decreases membrane performance, shortens its operational lifespan,[7,8] and often necessitates replacement of membranes.[9] To extend membrane operational lifespan, various anti-fouling strategies have been developed. Preventive approaches include pretreatment methods such as chemical coagulation[10] and aeration[11] of the feed, as well as surface modification of membranes using nanomaterials,[12] hydrophilic polymers,[13] or antimicrobial agents,[14] which aim to reduce foulant adhesion and biofilm formation. When fouling persists, removal techniques such as physical

I. Gurbuz
Department of Process and Energy
Delft University of Technology
Leeghwaterstraat 39, Delft 2628 CB, The Netherlands
H. Bazyar
Department of Chemical Engineering
Delft University of Technology
Van der Maasweg 9, Delft 2629 HZ, The Netherlands
A. Hunt
Department of Precision and Microsystems Engineering
Delft University of Technology
Mekelweg 2, Delft 2628 CD, The Netherlands
E-mail: a.hunt@tudelft.nl

The ORCID identification number(s) for the author(s) of this article can be found under https://doi.org/10.1002/adfm.202520484

DOI: 10.1002/adfm.202520484

Table 1. An overview of previously reported mechanically agitated filtration membranes and their anti-fouling performance.

Membrane	Electrodes	Operation	Construction and performance	Refs.
$Mn/BaTiO_3$ t = 200-220 µm, p = 0.21 µm	Porous steel, external*	20 V 265 kHz ‡	Piezoceramic membrane is synthesized. Activation by external electrodes increased oil antifouling efficiency from 38.3% to 91.0%.	[17]
$BaTiO_3$ t = 200 µm, p = 0.47 µm	Meshed stainless steel, external*	20 V 100 kHz ‡	Piezoceramic membrane (d_{33} of 55 $pC \cdot N^{-1}$) is synthesized. Agitation improved stable permeability for oil in water emulsions, Al_2O_3 suspensions and yeast suspensions by up to 12%, 82% and 30%, respectively.	[20]
PC/PZT t = 250 µm (PC), 200 µm (PZT), p = Non-porous(PC)	Readily embedded on PZT actuators	10 V 100–8000 Hz ‡	PZT actuators glued to corners of non-porous polycarbonate micromembrane. Agitation reduced bacterial adhesion by at least 88.2% and delayed biofouling growth by ca. one week.	0.7 cm[22]
PZT t = 200 µm, p = 300 µm	Meshed stainless steel, external*	20 V 190 kHz ‡	Piezoceramic membrane is synthesized. Agitation stabilized the steady-state permeance at ca. 71% of the initial value.	[23]
PZT t = 130 µm, p = 0.37 µm	Meshed stainless steel, external* †	10 V 1–200 kHz	Piezoceramic membrane is synthesized. Agitation with intermittent pulses prevented reduction in water flux during 3 hours of filtration.	[24]
PVDF t = 123 µm, p = 0.22 µm	Porous steel, external*	10 V 500-1000 Hz	Commercial membrane is poled. Agitated membrane produced ca. 40% of the initial flux after 7h, compared to ca. 10% in the passive control.	[26]
PVDF t = 52 µm, p = 140 µm	Sputtered Au on PVDF	24 V 1–4500 Hz	Non-porous commercial film is pin-punched to form porous membrane and sputtered with Au electrodes. Agitation produced 87 ± 3% higher permeate flux than the control after 30 min of filtering 0.5 g/L kaolin suspension.	[25]
PVDF-DMF t = 49 µm, p = 51 nm	Stainless steel, external*	10 V 500 Hz	Membrane is synthesized, poled and introduced to colloidal silica solution. Agitation reduced fouling progression by 66%, improved the critical flux by 25–46% and extended filtration duration by ca. 3x.	[19]
PVDF/graphene t = 400 µm, p = 60 nm	Cu foil	36 V N A	Membrane is synthesized and introduced to bovine serum albumin solution. Original permeance was maintained throughout the 120 min fouling tests, while the passive control exhibited a continuous decline.	[27]
Alumina/PZT t = 30 µm (Alumina), 100 µm (PZT), p = 0.2 µm	Sputtered Au on PZT	100 V 1–100 kHz	PZT actuators are synthesized and glued to the commercial alumina-coated ceramic membranes. Agitation reduced the flux decline by 59% during humic acid fouling.	[28]
Quartz t = 12 µm (SiO_2), 200 µm (ZrO_2), p = 2.6 µm (SiO_2), 270 nm (ZrO_2)	Stainless steel, external*	100 V 191 kHz	Porous quartz membrane is produced via solid-state synthesis and introduced to TiO_2 suspension. Agitation reduced the cake layer thickness from 64.2 µm to 48.4 µm over 200 min experiments.	[21]

Active parts of membranes: t = thickness and p = pore size * Part of the filtration module † Located 1 mm away from the membrane ‡ Resonance condition.

cleaning (e.g., backwashing)[15] and chemical cleaning[16] are applied. However, frequent reliance on physical and chemical cleaning increases treatment costs, necessitates operational breaks due to additional processing steps[17] and accelerates membrane degradation.[7,8] Developing antifouling membranes with high productivity and rejection ability remains a challenging endeavor requiring novel methods[18] to make membrane filtration technology economically and environmentally viable.[6]

Embedding vibratory self-cleaning functionality in filtration membranes can enhance[17,19] or even replace existing anti-fouling methods. This approach has been studied using piezoceramics,[17,20–24] piezoelectric polymers,[19,25,26] and their blends,[27] as summarized in **Table 1**.

Ceramic membranes based on $BaTiO_3$,[17,20] PZT,[23,24] alumina,[28] and quartz[21] have demonstrated effective antifouling performance. Active $Mn/BaTiO_3$ and $BaTiO_3$ membranes have respectively shown 2× (86% over 3 h) and 1.12x (82% over 1 h) flux increase compared to the passive controls,[17,20] while PZT-based membranes have shown a 1.28x (101% over 2.5 h)[24] and a 1.33x (81% over 3 h)[23] improvement. Actuating porous alumina membranes with PZT actuators from the corners has shown a 2× improvement in flux (6% over 2 h),[28] while PZT-based agitation of non-porous polycarbonate plates reduced bacterial adhesion by 88% (1 week delay in biofouling).[22] Utilization of ceramic membranes is limited by their brittleness and cost,[29] while PZT membranes further suffer from Pb leakage[30] and quartz requires very high driving voltages.[17]

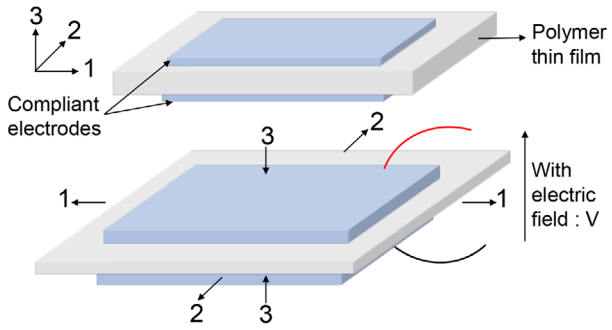

Figure 1. Electrostrictive actuation principle exhibited by P(VDF–TrFE–CTFE). Upon electrical stimulation, the film thickness (direction 3) decreases while its in-plane dimensions (directions 1 and 2) increase (inspired from ref. [35]).

Membrane separation technology mostly employs polymeric materials due to their superior processability, cost-effectiveness, abundance,[31] and mechanical flexibility.[32] To date, only PVDF[19,25,26] and its blends[27] have been employed to activate the polymeric membranes. Compared to passive controls, external electrode activation has shown a 200% flux increase over 7 h in PVDF membranes,[26] a 300% increase over 2 hours in PVDF/graphene membranes,[27] and a 3× longer lifespan in PVDF-DMF membranes.[19] Employing embedded electrodes on PVDF sheets with pin-punched pores (140 µm) has demonstrated an 87% improvement in flux over 30 min,[25] while the pore miniaturization remains constrained. As a limitation, pure PVDF exhibits low transduction efficiency and requires additional stretching and poling to induce piezoelectric behavior.[33]

In real wastewater, the presence of ions and contaminants introduces electrical conductivity, which, combined with the low electrical insulation of many membrane materials, can lead to short-circuiting and accelerated degradation during extended operation. Although agitation has generally proven effective in delaying fouling, the development of more electrically robust, chemically stable, and responsive materials, as well as efficient active membrane topologies, is required for practical implementation.

This research proposes a novel active filtration membrane concept, where electroactive polymer actuators are directly patterned on microporous filtration membranes for embedded agitation (see **Figure 1** for schematic illustration). Commercial PVDF and PTFE microporous membranes are combined with P(VDF–TrFE–CTFE) actuators that exhibit high strains without requiring pre-stretching or poling,[34] as detailed in Section 2.1. Design of the actuator patterns divides the membrane into actuation and filtration areas to locally stimulate the vibration modes during filtration, as explained in Section 2.2. Actuation patterns are fabricated by spray-printing inks of P(VDF–TrFE–CTFE) and carbon black (CB) that form the layers of insulation, actuation and electrodes, as explained in Section 2.3. The morphology and dynamic behavior of the resulting active membranes are further characterized following Section 2.4. Membrane dynamics is studied with respect to the substrate material, actuator positioning and layer thickness, measuring the average and localized surface accelerations. Experiments are conducted on a free membrane, and foulant removal is mimicked using dry metal alloy particles and Iriodin suspension (1 wt%). The results are presented and discussed in Sections 3 and 4 concludes the study.

2. Experimental Section

2.1. Materials

Active membrane design bases on commercial PTFE and PVDF membranes (Section 2.1.1), electroactive P(VDF–TrFE–CTFE) polymer (Section 2.1.2) and conductive carbon black electrodes (Section 2.1.3). PVDF Durapore microfiltration membranes (VVHP01205) and PTFE Omnipore membranes (JCWP14225) were procured both from Merck Life Science N.V., the Netherlands. Metalon JR-700HV ink with a 5 wt% loading factor was acquired from Novacentrix, USA. Piezotech RT-TS poly(vinylidene fluoride-trifluoroethylene-chlorotrifluoroethylene) (P(VDF–TrFE–CTFE)) powder was purchased from Arkema, Germany. Dimethyl sulfoxide (DMSO) and methyl ethyl ketone (MEK) were procured from Sigma-Aldrich, the Netherlands. For the sample holder components, stainless steel sheets (1.5 mm and 1 mm thick) were purchased from Metals Warehouse, United Kingdom. High-temperature-resistant resin and PLA filament were purchased from Formlabs, United States, and RS Components, the Netherlands, respectively. High-voltage-resistant cables and copper tape were purchased from RS Components, the Netherlands. Solid particles, including metal alloy balls ($Sn_{96.5}Ag_3Cu_{0.5}$) with 200 µm diameter), were procured from Shenzhen Qunwei Semiconductor Materials Co., China, and Iriodin 153 Flash Pearl Powder (20–100 µm diameter) was purchased from EMD Electronics- Merck Group, Germany. The suspensions were prepared using deionized water (18.2 MΩ · cm). All chemicals were used as received without additional treatment or purification.

2.1.1. Porous PVDF and PTFE Membranes

PVDF and PTFE are widely employed filtration membranes with well-established filtration characteristics, and key characteristics of the procured membranes are summarized in **Table 2**. The size of the pores was provided by the manufacturer, the thickness of the membrane was measured using a Mitutoyo 293-240-30 External Micrometer, and the mean flow pore (MFP) size was measured using a Porolux Revo Porometer (details given in Supplementary Information and Figure S1, Supporting Information).

Table 2. Characteristics of the employed filtration membranes. Pore size was provided by the manufacturer. Membrane thickness was measured using a Mitutoyo 293-240-30 External Micrometer by averaging 10 measurements taken from various spots on the membranes, with standard deviations included. The mean flow pore (MFP) size was determined using a Porolux Revo Porometer, based on the average of 3 measurements per membrane, and reported with standard deviations.

Membranes	Pore size [µm]	Thickness [µm]	Mean flow pore size [µm]
PTFE	10	73.27 ± 2.56	4.01 ± 0.11
PVDF	0.1	100.56 ± 1.42	0.25 ± 0.03

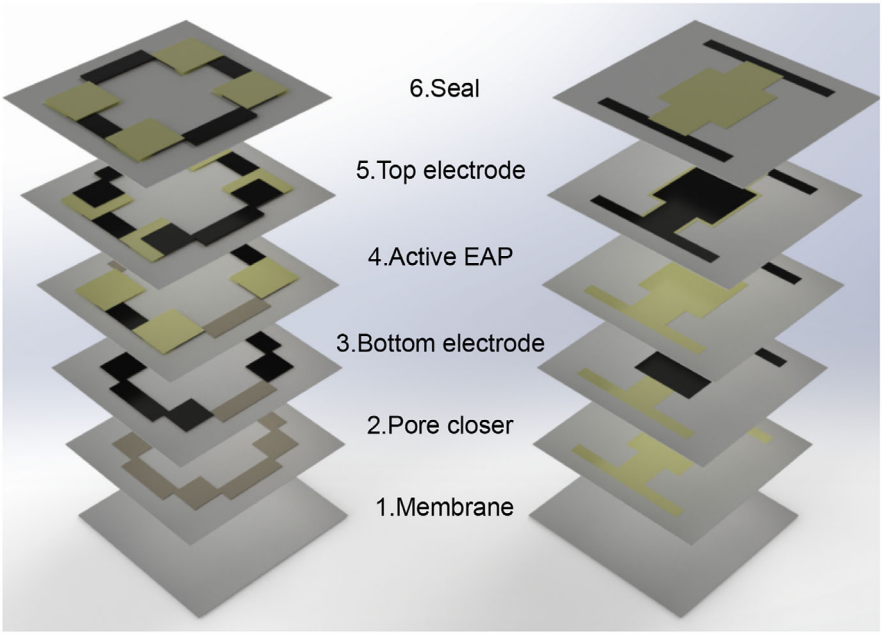

Figure 2. Schematic representation of the two different membrane-actuator configurations. Left: *4-corners* actuator, right: *central* actuator design. Both designs consist of identical functional layers, including microfiltration membrane, pore-closer layer, bottom electrode, electroactive polymer, top electrode, and seal.

2.1.2. Electroactive Polymer

Filtration membranes were agitated in this study by P(VDF–TrFE–CTFE) (i.e. poly(vinylidene fluoride-trifluoroethylene-chlorotrifluoroethylene)) that exhibits strong actuation performance[36] and does not require the elaborate pre-stretching or poling steps.[34] P(VDF–TrFE–CTFE) is a relaxor ferroelectric (materials with strong induced polarization and low remnant polarization) that exhibit high strains (ca. 5%), dielectric constant (up to 60), breakdown strength ($\geqslant$350 Vμm^{-1}), stable properties and a comparable elastic modulus to the membrane materials (up to 300 MPa).[33,34,37] P(VDF–TrFE–CTFE) of this study (Piezotech RT-TS) has a molecular weight of 400–600 kg mol^{-1}, a relative dielectric permittivity of 30–60 (at 1 kHz), and a Young's modulus of 0.1–0.5 GPa. It exhibited an electrostrictive coefficient (M_{31}) of 5–10 nm^2 V^{-2}, maximum strains of 2–5%, and an elastic energy density of up to 0.3–1 J cm^{-3}.[37]

For spray printing, an EAP ink was formulated by dissolving 5 wt% the P(VDF–TrFE–CTFE) in a 90:10 (v/v) MEK:DMSO mixture. MEK provided strong solubility but caused nozzle clogging due to its high volatility (boiling point 80 °C). This was mitigated by adding DMSO that exhibits higher boiling point (189 °C).[38] Increasing the DMSO fraction led to residual solvent and extended drying times, whereas lower fractions increased clogging. Polymer concentrations above 5 wt% resulted in non-uniform spray patterns.

2.1.3. Conductive Ink

Carbon black (CB) inks were employed for electrode fabrication as they have proven suitable for EAP actuators and compatible with spray printing.[38] Viscosity of 8.8 cP (25° C) and carbon nanoparticle size of 121 *n*m (z-average from dynamic light scattering method) were specified for the Metalon JR-700HV ink by the manufacturer.[39] The relatively large particle size reduces potential health risks, and the ink becomes conductive after solvent evaporation.[38]

2.2. Active Membrane Design

The Inkscape Vector Graphics Editor was used to design each layer of the actuators and further generate the G-code that contains instructions for the spray printer. Two different actuated membrane configurations were designed as illustrated in **Figure 2**, further addressed as the *4-corners* and *central* designs. Both designs consisted of the same functional layers: 1) a PVDF or PTFE filtration membrane, 2) a P(VDF–TrFE–CTFE) pore-closing layer, 3) the bottom electrodes, 4) the active P(VDF–TrFE–CTFE) layer, 5) the top electrodes, and 6) the P(VDF–TrFE–CTFE) sealing layer. Carbon nanoparticle ink (Metalon JR-700HV) was used to form the electrodes (layers 3 and 5). P(VDF–TrFE–CTFE) ink (5 wt% in a 90:10 MEK:DMSO solvent) was employed for both the actuation (layer 4) and interfacing (layers 2 and 6) purposes, providing electrical insulation from the wet environment.

2.3. Fabrication

An automated spray-deposition 3D printer[38,40] was employed to deposit the carbon black electrodes and PVDF terpolymer ink. The setup, illustrated in **Figure 3**, includes a two-fluid atomizer (comprising a solenoid valve and airbrush), a 3D printer platform, an air supply, a fume extractor, a printer controller, and

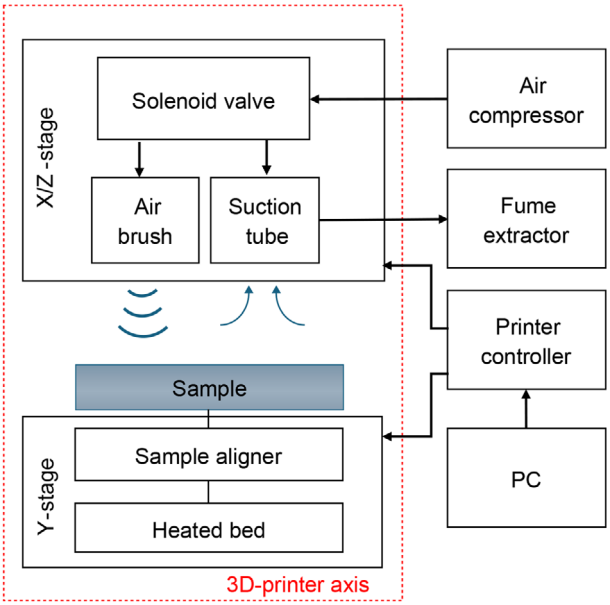

Figure 3. The working principle and main components of the custom-made airbrush spray printer.

a PC. Photographs of the printer axis components, the sample holder parts, and a microfiltration membrane mounted on the metallic holder are provided in Figure S2 (Supporting Information).

Both the *4-corners* and *central* actuator designs of the active membrane (Section 2.2) were spray-printed following the process explained in **Figure 4** using settings summarized in **Table 3**. The printing process involved five steps. First, a pattern of PVDF terpolymer ink was deposited, dried, and densified by heating at 130 °C for 2 h to locally close the pores in the membrane under the actuators. Next, carbon black ink was deposited and dried at 80 °C for 12 h to form the bottom electrodes. This was followed by deposition of the PVDF terpolymer solution, which was dried at 80 °C for 12 h. Then, carbon black ink was deposited to pattern the top electrodes, and dried at 80 °C for 12 h. Next, the PVDF terpolymer ink was printed over the electrodes to provide electrical isolation and prevent dissolution of the water-based carbon electrodes, thereby ensuring stable operation. Lastly, the membrane was annealed at 111 °C for 3 h. This served to eliminate any remaining solvent residues and improve the semi-crystalline structure of the EAP, thereby enhancing its relaxor ferroelectric properties.[38]

All functional layers were printed at a bed temperature of 80 °C and a 5-min waiting period was applied after the deposition of each functional layer to promote efficient solvent evaporation during printing and mitigate material spreading. The completed samples were placed in an oven at 80 °C overnight to remove any remaining residual solvents. Effective drying of the printed layers was confirmed by observing the transition of the carbon black and EAP layers from a glossy to a uniformly matte appearance. Photographs of the *4-corners* and *central* membrane actuator designs are provided in Figure S3 (Supporting Information).

Parameters in the spray-printing process include printing speed, air pressure, airbrush height, needle retraction, and print repetitions as specified in Table 3. Contribution of these parameters and development of the print process are further detailed in Supporting Information and ref. [38].

2.4. Experimental Characterization

2.4.1. Membrane Actuation Module

To fix the active membrane and tension it, a custom sample holder was designed, as explained in **Figure 5**: 1) the membrane was first clamped in the membrane holder between the backplate and the screwplate, 2) then the membrane was tensioned using a spacer that presses into the membrane when the tension plate is fastened to the screwplate, and 3) finally the tensioned membrane was pressed against the electrical contacts on the activation unit as the assembly was fastened to its frame.

All components were modeled in SolidWorks 2024. The backplate and screwplate were cut out of 1 mm and the tension plate was cut out of 1.5 mm thick plate of stainless steel using a laser cutter (Lion Lasers, Lion Alfa Metal XL). The spacer was made of Formlabs High Temp Resin and printed on Formlabs Form 4 3D printer. The activation unit was 3D printed using a Prusa i3 MK3 3D printer utilizing a Polylite PLA filament. Copper (Cu) electrodes were adhered to the designated recesses on the frame and electrically wired through designated openings, enabling the application of electrical input to the membrane actuators.

2.4.2. Actuator Components Characterization

The actuator components were analyzed in both the electrical and mechanical domains. In the electrical domain, key parameters affecting the actuator's performance include the resistance of the top and bottom electrodes, as well as the resistance between them. The samples for resistance characterization were fabricated using the same printing parameters listed in Table 3, in rectangular patterns with dimensions $a = 20$ mm and $b = 15$ mm. Print repetitions of 1, 2, 4, 8, 12, and 16 were applied. Figure S4 in the SI displays the rectangular sheets with the corresponding electrode layers. The bottom electrodes were printed on pore-closed membranes, which had three print repetitions of the EAP layer, while the top electrodes were printed on an EAP layer with sixteen print repetitions to mimic the structure of membrane actuators.

A photo of the 4-point probe setup used for these measurements and the schematic of its working principle are shown in Figure S5 (Supporting Information). The setup consists of a probe head (SP4, Signatone) with a 1.5875 mm spacing between the probes, a current source (2400 SourceMeter, Keithley), and a nanovoltmeter (2182 Nanovoltmeter, Keithley). A 10 µA current was applied, and the probe tips were positioned at the center of each sample to measure the resulting voltage drop.

Given that the probe electrode spacing is significantly larger than the electrode thickness t (ranging from ca. 1 µm to 16 µm, depending on the number of printed layers), yet much smaller than the sample dimensions, the sample sheet resistance (R_s) can

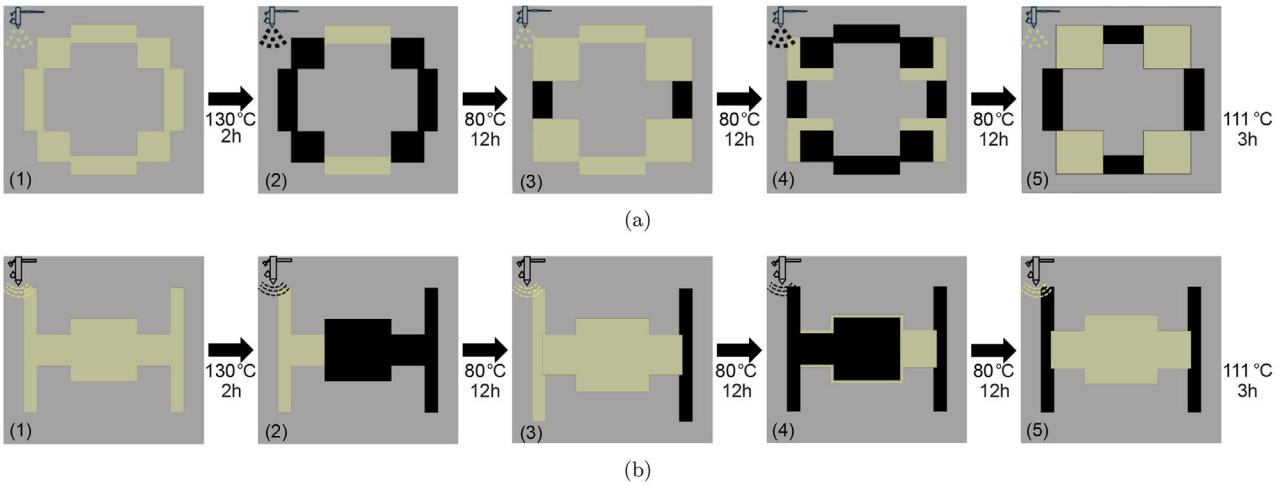

Figure 4. Spray-printing procedure for a) *4-corners* actuators and b) *central* actuators. Deposition steps are as follows: 1) P(VDF–TrFE–CTFE) polymer, followed by 2 h of melting at 130 °C; 2) Carbon black, followed by 12 h of drying at 80 °C; 3) P(VDF–TrFE–CTFE) polymer, followed by 12 h of drying at 80 °C. 4) Carbon black, followed by 12 h of drying at 80 °C; 5) P(VDF–TrFE–CTFE) polymer, followed by 3 h of annealing at 111 °C.

be determined using the geometric correction factor $R_1 = 0.9223$. The calculation is expressed as:

$$R_s = \frac{\rho}{t} = \frac{V\pi R_1}{I\ln(2)} \approx 4.18\frac{V}{I} \quad (1)$$

where ρ represents the electrode resistivity, I is the applied current, and V is the measured voltage.

The resistances of both the bottom and top electrodes, as well as the resistance between them, were measured on the membrane actuators using a Digital Multimeter (Voltcraft VC150-1).

In the mechanical domain, key parameters investigated included membrane structure and morphology, as well as the thickness and uniformity of the deposited layers. To expose the membrane cross-section, a femtosecond laser micromachining system (Lasea LS Lab, Pharos PH1 source) was used. The samples were then sputter-coated with a ca. 18 nm thick gold layer (Jeol JFC-1300, 20 mA for 30 s at 25 mm distance) and imaged in scanning electron microscopy (SEM, Jeol JSM6010LA). The pristine membranes and the individual components of the active membranes were imaged to characterize their surface morphologies and cross-sections, for both the PVDF and PTFE base membrane materials.

2.4.3. Actuation Characteristics

The active membrane actuation characteristics were studied using a laser doppler vibrometer (LDV, Polytec PSV-400), allowing to measure the magnitudes and phases of motion over the surface of the membrane. As shown in **Figure 6**, the actuation module is placed under the scanning head of the LDV system and actuated via a high-voltage amplifier (Smart Materials HVA 1500-50). Experiments are controlled, processed and stored by the PSV Acquisition software from a PC computer (Polytec DMS). A digital oscilloscope is used validate the applied signals during experiments.

The experiments were set up to measure a 9x9 grid of 81 points, equally spaced over the membrane surface. Surface velocities at these points were measured by exciting the active membrane with a frequency sweep of 50 to 8000 Hz at amplitudes ranging from 150 V to 700 V. Reference measurements were conducted to establish the level of noise by disconnecting the voltage amplifier. The measured velocities were further used to calculate the accelerations for each of these point and their averages. Mode shapes were visualized at the frequencies that correspond to the peaks in the average acceleration response plots.

Dynamics of a filtration membrane was analysed in Comsol Multiphysics 6.2 to identify the shapes of its vibration modes and compare them to the experimental findings. The *4-corner* design (Figure 2) of PVDF and PTFE microfiltration membranes (30 × 30 mm^2 square) were clamped on the edges, pre-tensioned (in-plane static body load of 10^5 Nm^{-3}) and analyzed in an eigenfrequency study.

2.4.4. Particle Manipulation

Solid particle manipulation induced by membrane activation was examined using two imaging methods, as illustrated in Figure 6:

Table 3. Printing parameters for actuator layers: bottom insulator (pore-closer layer), electrodes, active EAP and top insulator (seal).

	Functional layers			
Print parameters	Bottom insulator	Electrodes	Active EAP	Top insulator
Bed temperature [°C]	80	80	80	80
Printing speed [mm s^{-1}]	1500	1500	1500	1500
Pressure [psi]	20	10	20	20
Airbrush height [mm]	6	5	8	8
Needle retraction [mm]	−0.60	−0.20	−0.60	−0.60
Print repetitions	3	16	16/32/64[a)]	3

[a)] Varies between samples.

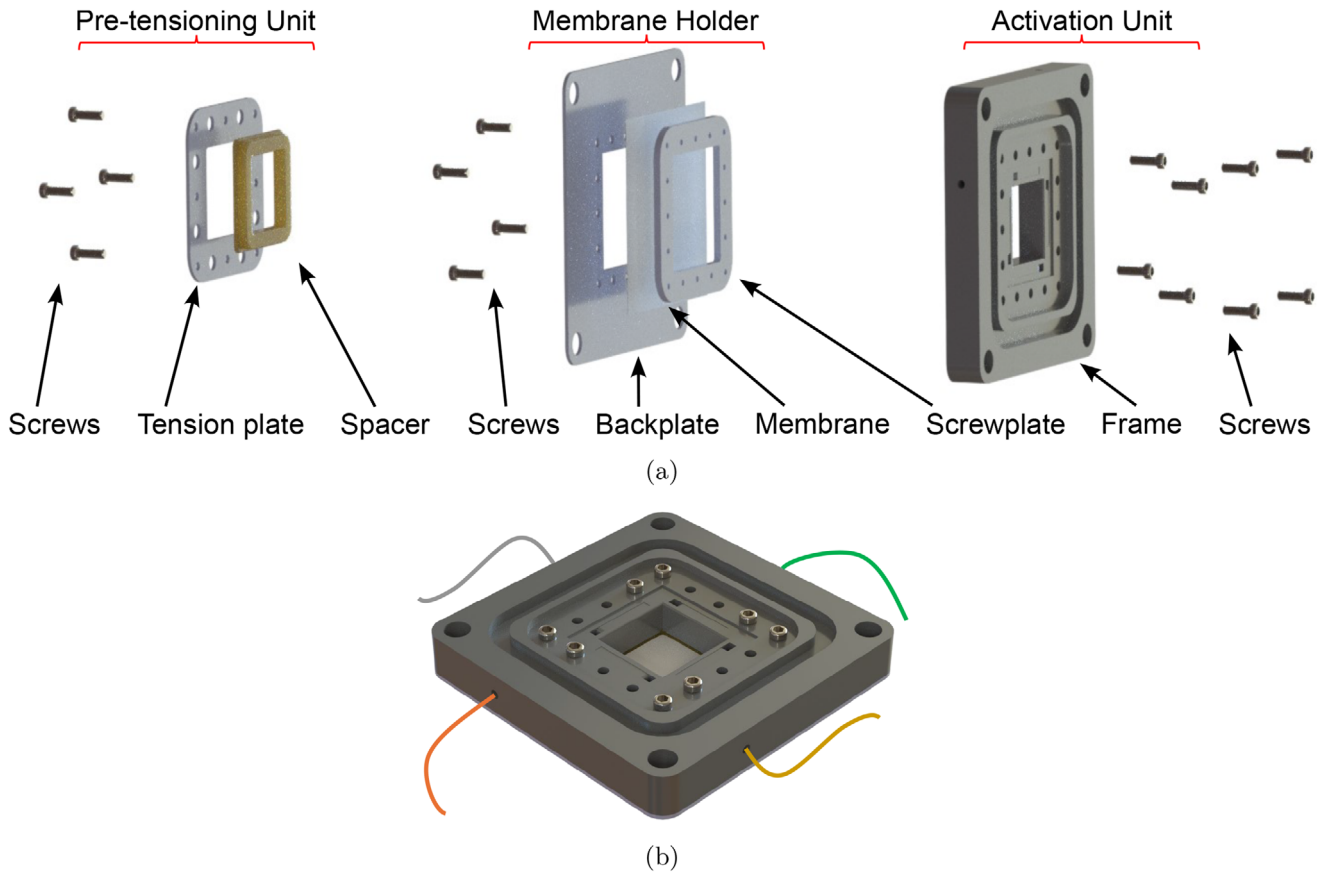

Figure 5. Construction of the membrane actuation module: a) Exploded view, and b) Assembled module. The module consists of metallic plates (backplate, screwplate, tension plate), 3D-printed components (spacer and frame), electrical conductors (copper electrodes and wires) and fastening screws.

a Toolcraft USB Microscope (2 MP, 200× digital zoom) and a Navitar Pixelink high-speed camera equipped with a 12× zoom lens. Actuation module was oriented such that the actuators remain on the bottom side, while top surface was randomly seeded with metal alloy balls of 200 µm diameter. The added mass altered the membrane resonant frequencies and they were therefore measured again using the LDV. Two resonant frequencies of highest average surface accelerations were identified for each active membrane for particle manipulation experiments. These were further used as the center frequencies of the continuously looping frequency sweeps (resonance 50 Hz, 0.64 s or 1.28 s duration) that were applied to the active membranes while recording the particle motion (USB Microcapture microscope).

A 1 wt% suspension of Iriodin 153 Flash Pearl was prepared to visualize the manipulation of particles in water. The suspension was applied on the active membranes and displacements of Iriodin particles were observed during membrane actuation were recorded (Navitar Pixelink Fast Speed Camera).

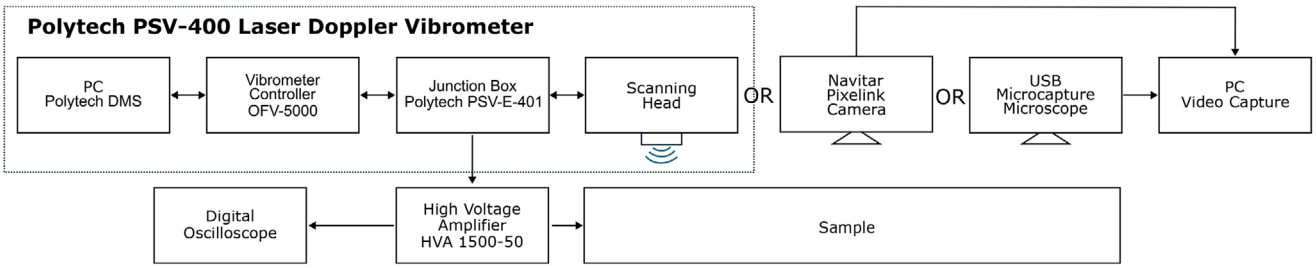

Figure 6. Experimental setup for characterizing the active filtration membranes. The Polytec PSV-400 LDV was used to activate the membrane actuators, characterize their actuation behavior, and perform modal analysis. Particle manipulation was visualized using a camera or a microscope, depending on the required resolution and field of view.

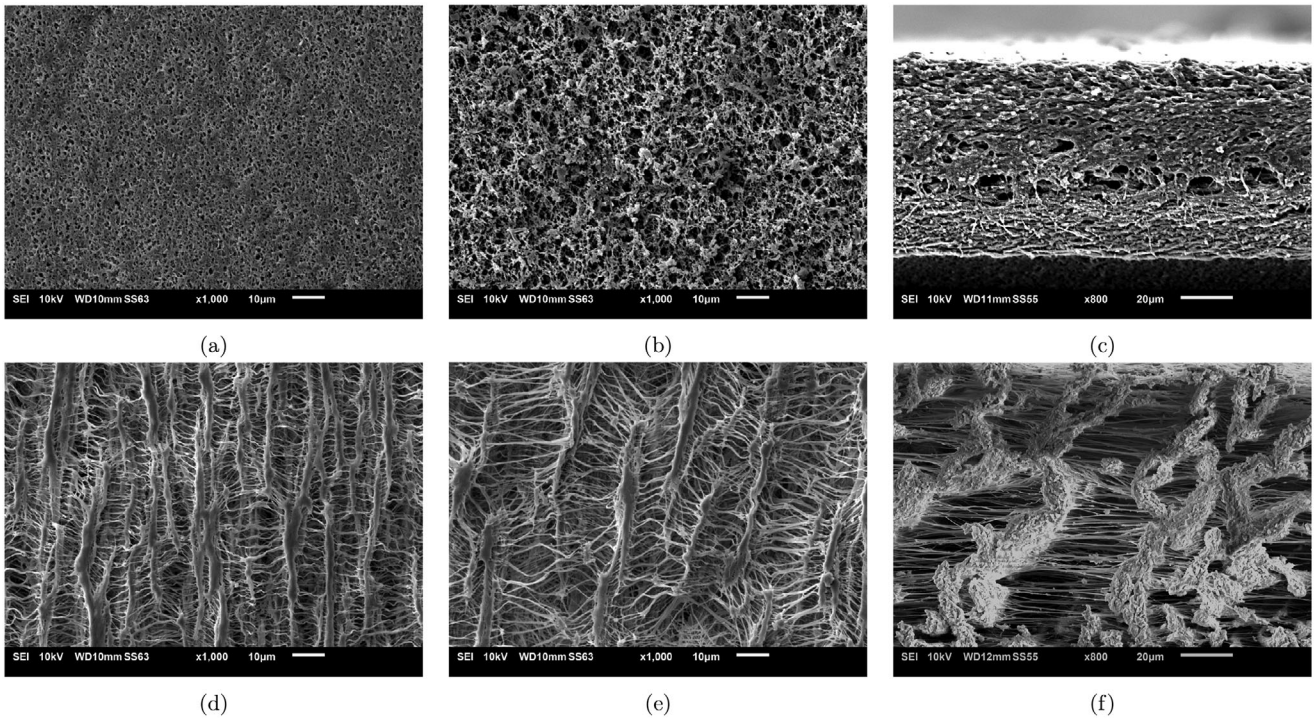

Figure 7. SEM images of pristine microfiltration membranes: The first row shows PVDF membranes from a) top view, b) bottom view, and c) cross-sectional view. The second row presents PTFE membranes from d) top view, e) bottom view, and f) cross-sectional view.

2.4.5. Statistical Analysis

Mean flow pore (MFP) size was determined with a Porolux Revo Porometer from three replicate measurements per membrane and reported as mean ± standard deviation (SD). Membrane thickness (PVDF and PTFE) and electrode sheet resistance were each measured ten times, with results expressed as mean ± SD. Membrane dynamics were characterized by surface velocity measurements during frequency sweeps (50–8000 Hz); velocities were averaged over three acquisitions by the PSV software and converted to surface accelerations. All datasets were visually inspected for anomalies, with no exclusions. Comparisons are descriptive, as no formal hypothesis testing was performed. Data analysis and visualization were conducted in MATLAB R2024b (MathWorks, Natick, MA, USA).

3. Results and Discussion

3.1. Membrane Actuator Characterizations

3.1.1. Morphology

Scanning Electron Microscopy (SEM) was performed to examine the morphology of the membrane actuator interfaces and assess layer uniformity, as described in Section 2.4.2.

SEM micrographs of the untreated commercial PTFE and PVDF membranes—including top surfaces, bottom surfaces, and laser-cut cross-sections—are shown in **Figure 7**. The micrographs indicate structural differences across various regions of the membranes, highlighting variations in porosity type, pore size, and anisotropy.

The SEM images of the PTFE and PVDF microfiltration membranes after deposition of the PVDF terpolymer solution demonstrate the effective pore coverage under the established printing parameters. Achieving proper pore coverage is essential to prevent short-circuiting when the membrane is submerged in aqueous media and to create a uniform surface for the deposition of the bottom electrode. Adequate pore coverage was achieved with a minimum of three print repetitions. However, complete elimination of local porosity was not feasible at room temperature. To address this, the PVDF terpolymer layer was densified by heating the membranes in an oven at 130 °C (above the melting point of the PVDF terpolymer of 122 °C[37]) for two hours. This treatment eliminated the remaining open pores and nonuniformities in coverage (see Figure S6, Supporting Information).

Surface morphologies of the printed electrodes are shown in **Figure 8**. The top electrodes display rougher surface textures than the bottom electrodes on both the PTFE and PVDF membranes, while no significant differences were observed between the same electrodes on different membranes. There was no significant differences observed in the morphology of the active and sealing layers of PVDF terpolymer (see Figure S7, Supporting Information).

SEM images of the cross-sections of the completed actuators were analyzed for both membrane types. **Figure 9** shows the cross-sections of the actuator regions on the PTFE and PVDF microfiltration membrane, and a zoomed-in view of the active layer. The layer thicknesses were measured from the micrographs: 1) microfiltration membranes 75-100 µm; 2) pore-closing layer

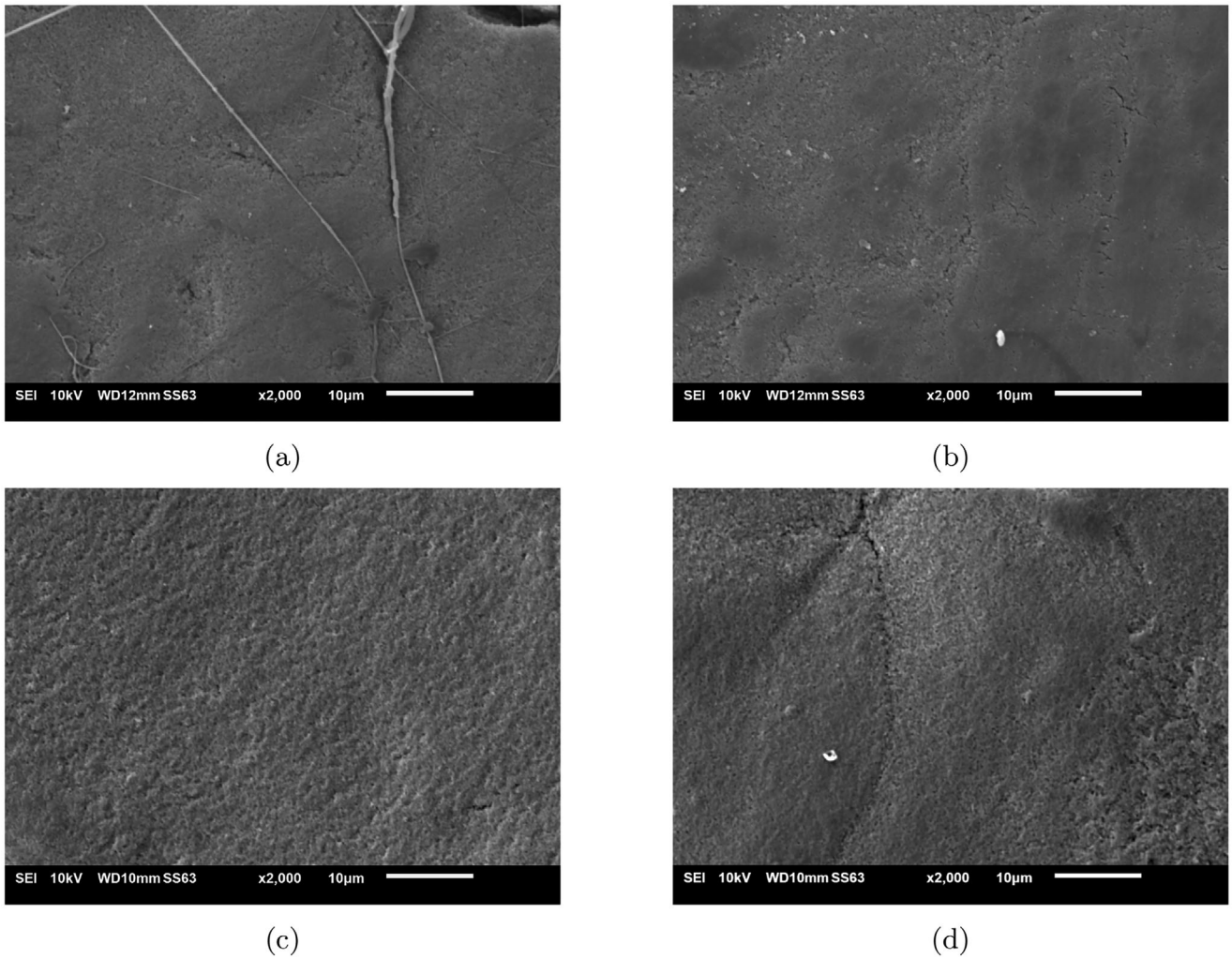

Figure 8. SEM images after electrode deposition: a) the bottom electrode on the pore closer layer of PTFE membranes, b) the bottom electrode on the pore closer layer of PVDF membranes, c) the top electrode on the active layer of PTFE membranes, and d) the top electrode on the active layer of PVDF membranes.

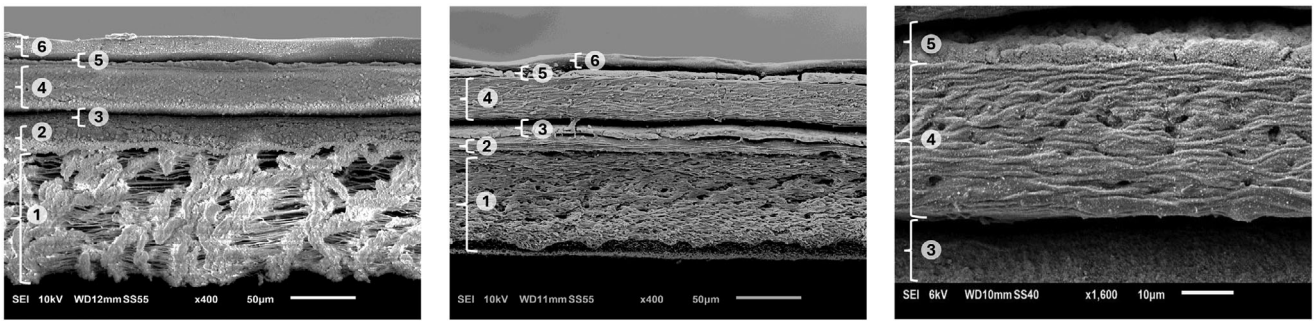

Figure 9. SEM images of the cross-section morphology of the active membranes at the site of actuators: a) a PTFE-based membrane, b) a PVDF-based membrane, and c) a zoomed-in view of the active EAP layer. The layers are labeled as follows: 1) microfiltration membrane (75–100 µm), 2) pore-closer (10 µm), 3) bottom electrode (12 µm), 4) electro-active polymer (25 µm), 5) top electrode (12 µm), and 6) seal (10 µm).

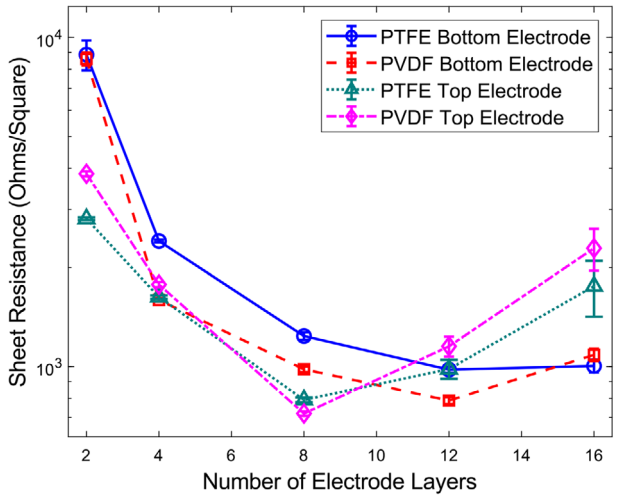

Figure 10. Sheet resistance of the top and bottom electrodes for PTFE- and PVDF-based actuators, reported as mean ± SD from 10 measurements per data point.

10 µm; 3) bottom electrode 12 µm; 4) electroactive polymer 25 µm; 5) top electrode 12 µm; and 6) the sealing layer 10 µm.

The printed actuators and electrodes covered a part of the filtration membrane, reducing its filtration capacity, as explained in Supporting Information and Figure S3 (Supporting Information). The functional actuators of the *4-corner* and *central* design respectively constituted 7% and 9% of the filtration membrane area, and all actuator components respectively covered up 33% and 25% of the membrane (i.e., closed pores).

3.1.2. Electrode Resistivity

Sheet resistance was measured as described in Section 2.4.2 and the relationship between the number of print repetitions and the resulting top and bottom electrode resistance (including corresponding standard deviations) is presented in **Figure 10**. Print repetitions of 1, 2, 4, 8, 12, and 16 were investigated, with the remaining printing parameters detailed in Table 3. No significant difference in electrode resistivity was observed between PTFE and PVDF microfiltration membranes, as the pores in both membranes were effectively sealed with the polymer (as shown in the SI, Figure S6). A single carbon ink layer was insufficient to fuse the droplets into a conductive sheet, while the resistance decreased with increasing print repetitions due to the cumulative deposition of the conductive carbon ink.

For the bottom electrodes, two print repetitions yielded a sheet resistance of ca. $0.9 \times 10^4\ \Omega\square^{-1}$. Increasing the number of repetitions to 12 significantly reduced the sheet resistance to ca. $1.0 \times 10^3\ \Omega\square^{-1}$, indicating a significant improvement in conductivity. However, further increasing the print repetitions to 16 resulted in a slight rise in sheet resistance relative to the 12-layer case. This counterintuitive trend is attributed to the accumulation of excess solvent during printing, which prolonged drying times and promoted ink spreading. As shown in Figure S4 (Supporting Information), 16 print repetitions produced irregular coverage rather than well-defined rectangular patches. Therefore, 12 print repetitions were identified as the optimal compromise, achieving low resistivity while minimizing processing time and material consumption. Prior studies have demonstrated that the sheet resistance of CB electrodes approximately doubles upon coating with P(VDF–TrFE–CTFE).[41]

For the top electrode, two print repetitions yielded a sheet resistance of ca. $0.3 \times 10^3\ \Omega\square^{-1}$. The minimum sheet resistance was achieved after 8 print repetitions, reaching ca. $0.7 \times 10^2\ \Omega\square^{-1}$, which represents the optimal conductivity achieved in this series. Beyond this point, further material deposition led to non-uniform ink distribution, thereby reducing electrode performance. To mitigate this effect, sufficient drying time between print repetitions is essential.

3.2. Membrane Dynamics

As explained in Section 2.4.3, the dynamics of the active membrane were analyzed with respect to actuator placement (Section 3.2.1), membrane material (Section 3.2.1) and actuator thickness (Section 3.2.2). Membrane surface accelerations were examined to assess both local and global dynamic behavior (Section 3.2.3). Membrane vibration modes were visualized using laser doppler vibrometer (LDV) and compared with COMSOL simulations (Section 3.2.4).

3.2.1. Actuator Placement and Membrane Material

The average surface accelerations for the actuated *central* and *4-corner* design actuators (see Figure 2) are plotted in **Figure 11a,b** in response to 150 V and 300 V sine wave sweeps (50–8000 Hz). The results for the PTFE and PVDF membranes are respectively compared in Figure S8a and S8b. As anticipated, doubling the actuation voltage (150 V to 300 V) produces ca. 4x higher strains and accelerations due to the quadratic strain-voltage relationship of relaxor ferroelectric transducers.

The *4-corners* design consistently produced higher peak accelerations than the *central* design, achieving up to 12 m s^{-2} on PTFE and 20 m s^{-2} on PVDF substrates. The *central* design reached up to 3 m s^{-2} on PTFE and 16 m s^{-2} on PVDF substrates upon the same excitation amplitude (300 V). While the *4-corners* design achieved higher peak surface accelerations at smaller actuator size (7% versus 9% of the membrane area), the design used up more effective filtration membrane area (33% vs 25%). It is hypothesized that the better performance of the *4-corners* design stems from better spatial co-location between the actuator placement and the locations of highest strains of the vibration mode shapes (see Table 5). This enables more efficient coupling of the actuation output to the resonant vibrations of the membrane.

PVDF membranes exhibit significantly higher surface accelerations than the PTFE membranes, hypothesized to stem from the lower damping and higher Q-factor of the homogeneous PVDF microstructure, in contrast to the anisotropic microfibrous PTFE, as seen in SEM images in Figure 7. PVDF further exhibits higher resonance frequencies in response to the identical stimulus, attributed to the higher Young's modulus (ca. 2.2 GPa[42] for PVDF and 0.4 to 1.8 GPa for PTFE[43]). This results in higher membrane tension under identical prestrain.

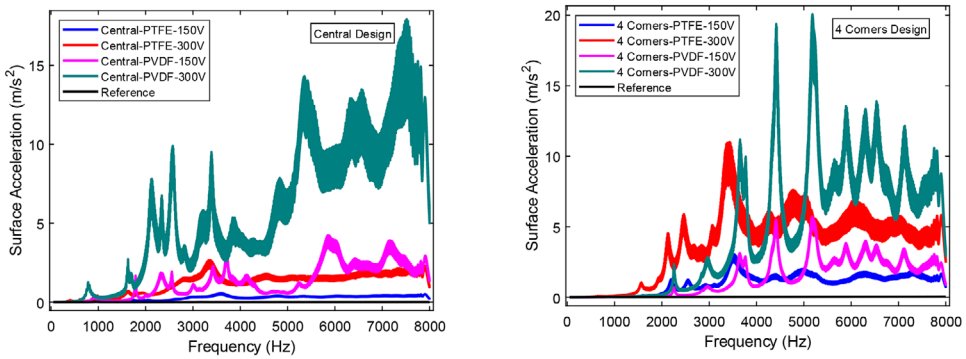

Figure 11. Spectra of the average surface accelerations in the active (a) *central* actuator design and (b) *4-corners* actuator design upon stimulation with 150 V_{pp} and 300 V_{pp} sine wave sweeps. References indicate noise floor measurements with actuation terminals disconnected. Reported spectra represent the average of three consecutive sweeps automatically computed by the PSV 9.2 Acquisition software.

3.2.2. EAP Layer Thickness

The *4-corner* design of the active PVDF membranes was fabricated at different EAP thicknesses (25 µm, 50 µm, and 100 µm), following the methodology described in Section 2.4.3. Average surface accelerations in response to 300 V stimulus are plotted in **Figure 12** and at maximum operating voltages (300 V for 25 µm, 600 V for 50 µm, and 900 V for 100 µm) in Figure 12. The maximum operating voltages of each design are defined as the highest voltages of reliable operation, without any indications of dielectric breakdown. These voltages were identified from the membrane actuation experiments, that were repeated by incrementally increasing the operating voltage in 50 V steps, until electrical discharges (visible sparks) were observed, indicating dielectric failure.

At 300 V excitation the membranes with the thinnest EAP layer (25 µm) exhibit the highest average surface accelerations 36.8 m s^{-2} due to the quadratic field-strain relation of the relaxor ferroelectric materials.[44] Near breakdown voltages the membranes with thicker EAP layer exhibited higher average surface accelerations, with up to 77.5 m s^{-2} and 74.5 m s^{-2} respectively for the 100 µm and 50 µm EAP layer (see Figure 12). While thicker EAP layers withstand higher voltages, the maximum permissible electric field strength remained between 9–12 V μm^{-1}, with the variation attributed to the fabrication imperfections. Normalizing the average surface accelerations by the applied voltage (see Figure S8, Supporting Information) indicates that the thickest EAP layer (100 µm) results in lower average acceleration per volt. This is hypothesized to stem from the higher stiffness of the thicker samples and possible lower film quality of thick EAP layers[35].

Increasing the thickness of the EAP layer adds mass to the membrane and therefore reduces its resonant frequencies. However, this impact cannot be seen in the results (**Table 4**) due to the stronger effect of membrane pre-tension and its variations among samples. Chemical stability is not expected to be affected by the EAP layer thickness, since the EAP (P(VDF–TrFE–CTFE)) and the membrane materials (PVDF and PTFE) have a similar molecular structure (highly fluorinated backbone) and are well-known for their inertness.

3.2.3. Localized Surface Vibrations

Local surface accelerations were studied based on the *4-corner* design (50 µm EAP, PVDF membrane), as described in

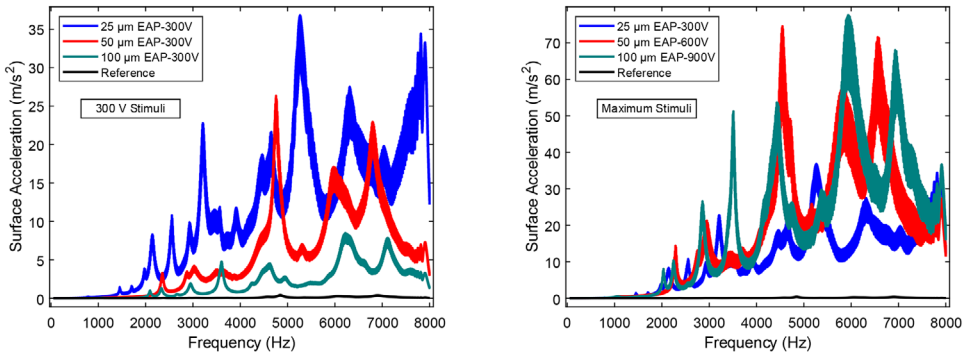

Figure 12. Average surface accelerations of the active membranes for different EAP layer thicknesses (25 µm, 50 µm, and 100 µm) at a) 300 V excitation and b) at the maximum voltages before breakdown (300 V for 25 µm, 600 V for 50 µm, and 900 V for 100 µm). References indicate noise floor measurements with actuation terminals disconnected. Reported data are averaged over three consecutive sweeps using the PSV software.

Table 4. Experimentally observed resonance modes/frequencies for the actuators investigated in Section 3.2. Each mode represents a distinct vibrational pattern, with variations influenced by actuator configuration, membrane material, and mechanical tension. Green and red indicate acceleration maxima in opposite directions and brightness signifies their magnitude.

	25 µm EAP				50 µm EAP	100 µm EAP
	PTFE Membranes		PVDF Membranes			
	central	*4-corners*	*central*	*4-corners*	*4-corners*	*4-corners*
1st Mode	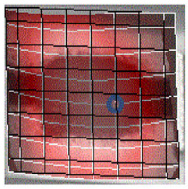 414 Hz	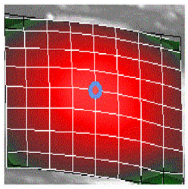 682 Hz	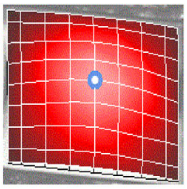 786 Hz	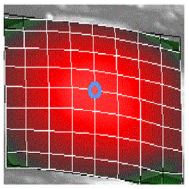 954 Hz	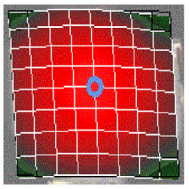 1076 Hz	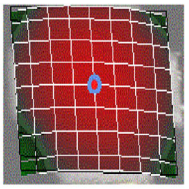 1121 Hz
2nd Mode	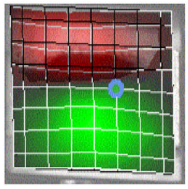 643 Hz	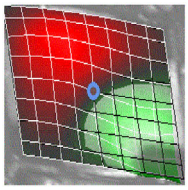 1565 Hz	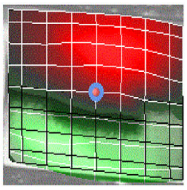 1628 Hz	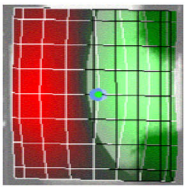 2254 Hz	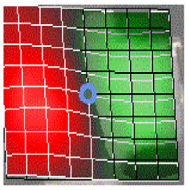 2287 Hz	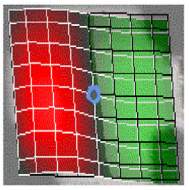 2245 Hz
3rd Mode	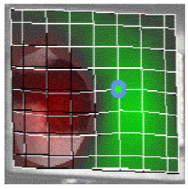 1032 Hz	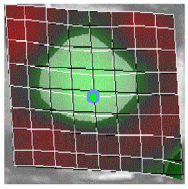 2465 Hz	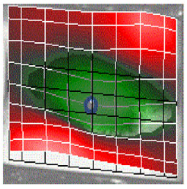 2131 Hz	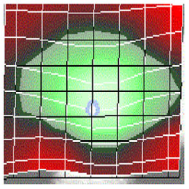 2968 Hz	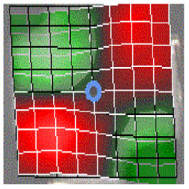 2751 Hz	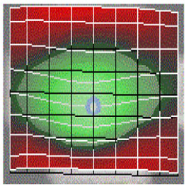 2857 Hz
4th Mode	 1731 Hz	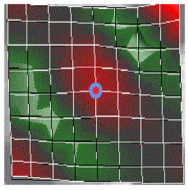 3426 Hz	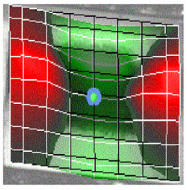 2575 Hz	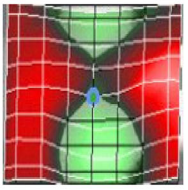 3771 Hz	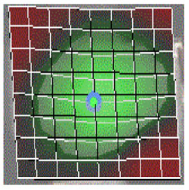 2926 Hz	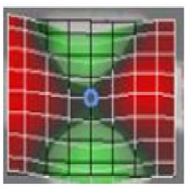 3512 Hz
5th Mode	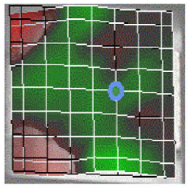 2059 Hz	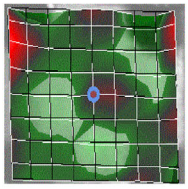 4767 Hz	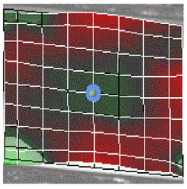 5356 Hz	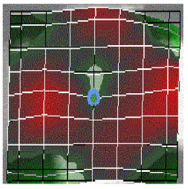 4415 Hz	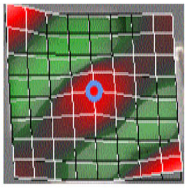 4548 Hz	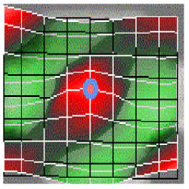 4426 Hz
6th Mode	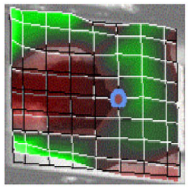 4834 Hz	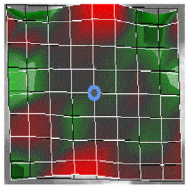 6093 Hz	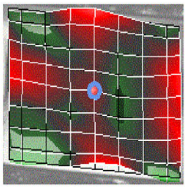 7517 Hz	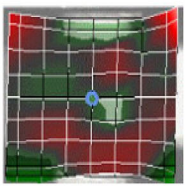 5181 Hz	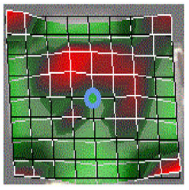 6560 Hz	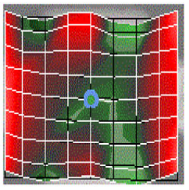 5932 Hz

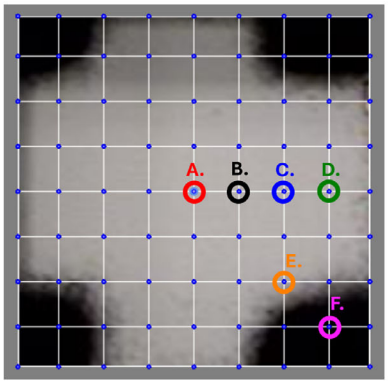

(a)

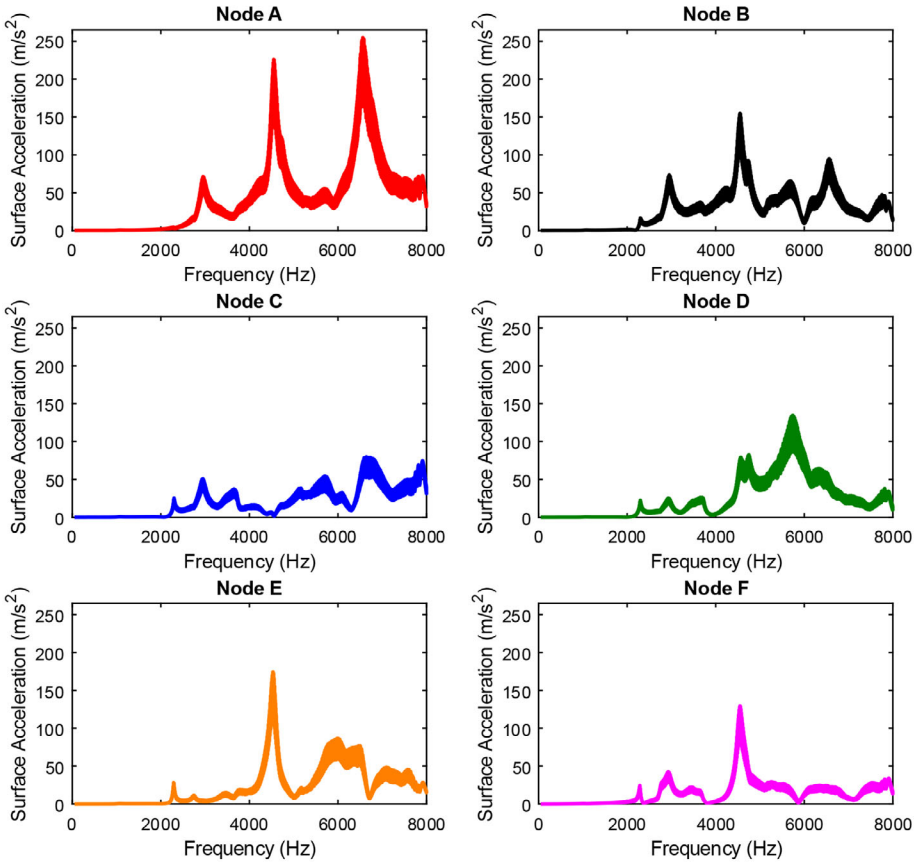

(b)

Figure 13. Local surface accelerations in a PVDF-based active membrane (50 µm thick EAP actuator) upon 600 V_{pp} excitation: a) node locations A–F on the membrane and b) surface accelerations at different nodes. Reported spectra represent the average of three consecutive sweeps automatically computed by the PSV software.

Section 2.4.3. Six nodes were selected in the measurement array (indicated as A to F in **Figure 13**) with their acceleration plotted in Figure 13. All the nodes showed 1.07 to 3.42 times higher surface accelerations than the membrane average in response to an identical stimulus (600 V). Node A showed up to 255 m s^{-2} accelerations at 6560 Hz in contrast to the average membrane acceleration of 71.5 m s^{-2} at the same frequency (Figure 12). This is an anticipated result since the membrane mobility is the highest at the center, while the average is lowered by the near-zero accelerations near the membrane boundaries. Beyond the first mode, the acceleration at each selected node further depends on its position relative to the specific mode shape (**Table 5**), particularly in regions of maximum strain.

Table 5. Simulation visualization of the mode shapes in a *4-corner* design of the active filtration membrane.

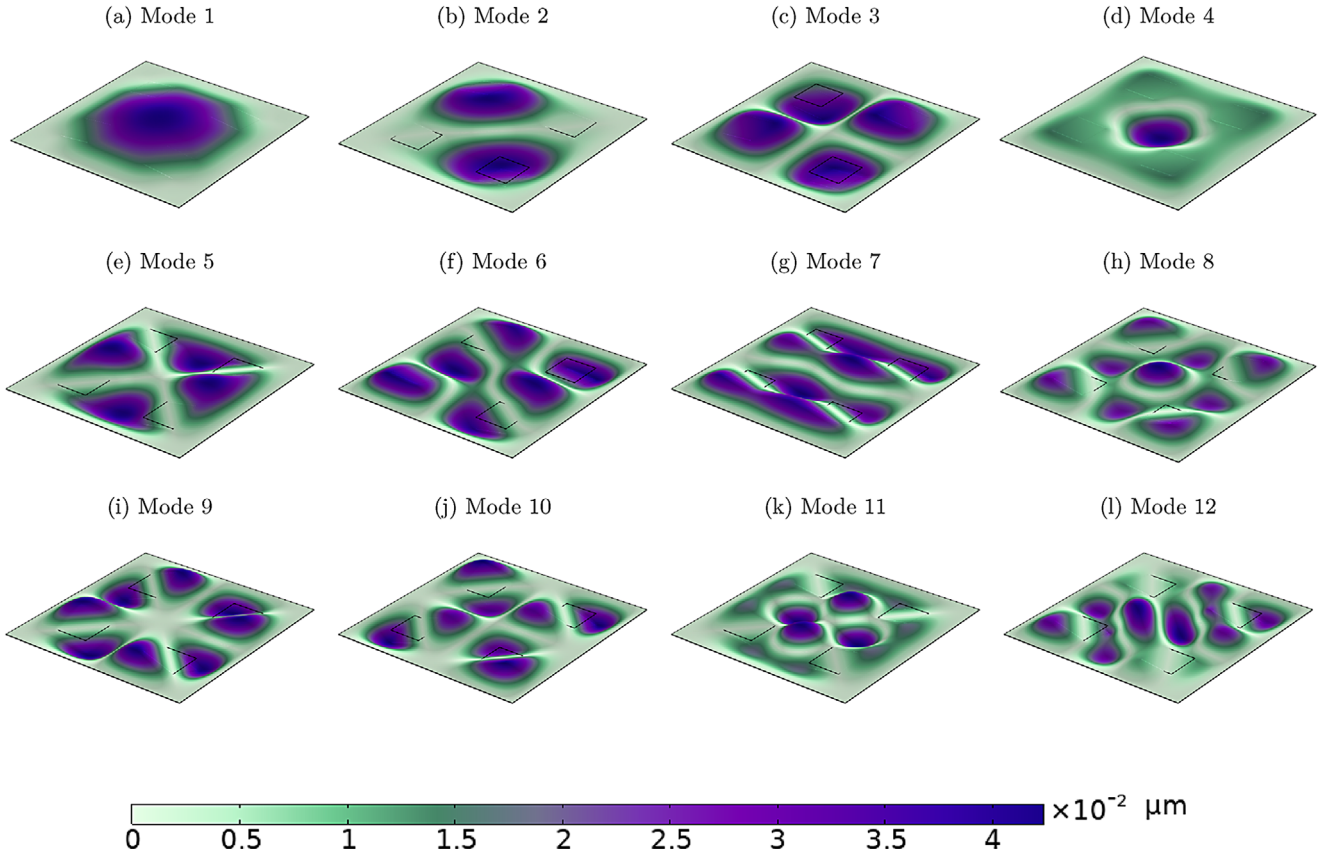

Scale bar for all modal shapes in Table 5

3.2.4. Modal Shape Analysis

Membrane dynamics was investigated numerically and experimentally according to the methodology described in Section 2.4.3. Simulation results for the first twelve eigenmodes of the *4-corner* active PVDF membrane design are presented in Table 5, whereas the *central* and *4-corner* designs showed no visually observable differences from the unaltered membrane dynamics. Experimental results for the first six eigenmodes and frequencies were determined from the acceleration magnitude plots (see Section 3.2) for each membrane material, design and EAP layer thickness and are visualized in Table 4.

In Table 4, the first modes of all the membranes correspond to the numerical estimation of Table 5. While a corresponding simulation (or its degenerative equivalent) can be identified for each of the measured modes, their sequence and exact shape may differ from the simulation prediction. Variations in shape arise from degenerative mode shapes of the symmetric membrane (90° rotation, removed from simulation results) and anisotropy in membrane tensioning (imperfections in implementation and anisotropy of the membrane material)[45,46] Further deviations are caused by the limited number of points in the LDV measurement grid (9x9), especially in the higher order modes that approach Nyquist limit in the spatial frequency. PVDF membranes displayed higher frequencies and magnitudes for the same eigenmodes than the PTFE membranes, attributable to the higher stiffness of the material and lower damping of their morphology (Section 3.2.1).[47,48]

3.3. Particle Manipulation

The particle manipulation performance of the active microfiltration membranes was investigated using the methodology outlined in Section 2.4.3. PVDF membrane with the *4-corner* actuator design of 25 μm-thick EAP layer was attached to the activation unit (actuators facing down) and **Figure 14** plots the surface accelerations from the frequency sweep experiments (300 V amplitude): 1) the free membrane in air; 2) the membrane covered with metal alloy spheres (**Figure 15**); 3) the membrane covered with water and metal alloy spheres; 4) the membrane covered in Iriodin 153 Flash Pearl suspension (**Figure 16**); and 5) the deactivated membrane to detect the noise floor. No delamination or structural deterioration was observed during the experiments.

The surface accelerations of unloaded membrane increased linearly with frequency at a slope of +2 m s^{-2} Hz^{-1}, exhibiting

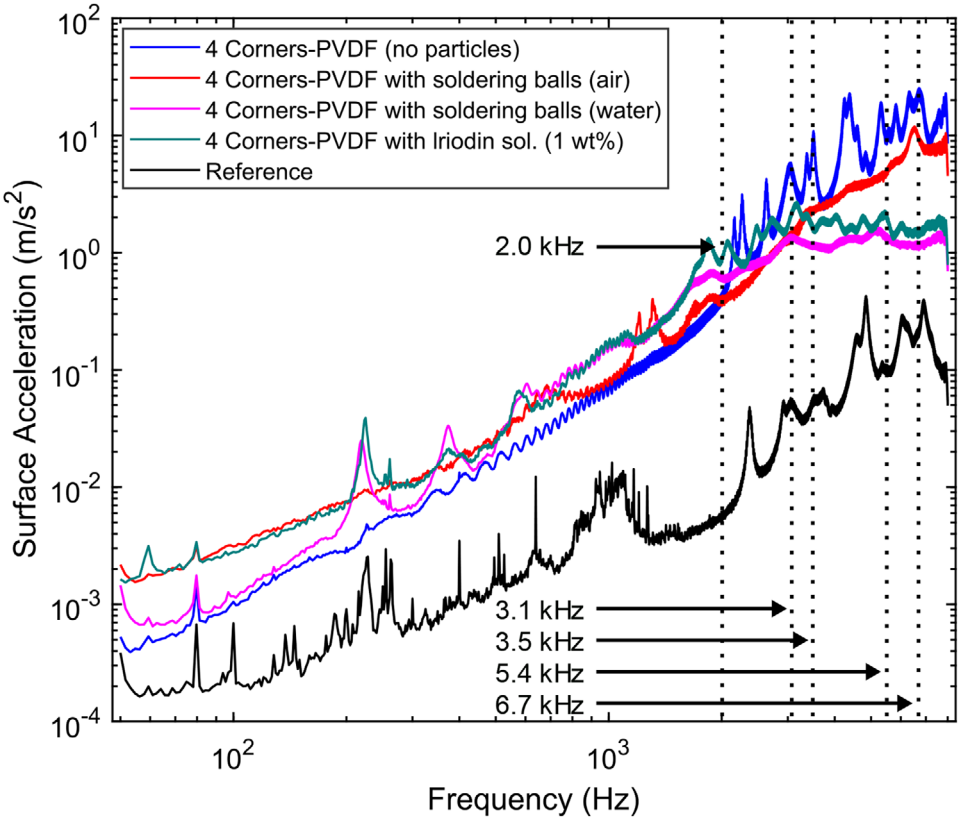

Figure 14. Comparison of surface accelerations in particle manipulation experiments (*4-corner* design, 300 V_{pp} stimulus) for the free membrane (blue line), dry memrbane with metal alloy balls (red line), wet membrane with metal alloy balls (magenta line), and membrane loaded with 1 wt% Iriodin suspension (teal line). Reference indicates noise floor measurements with actuation terminals disconnected (black line). Vertical dashed lines indicate agitation frequencies of the visualization experiments. Each spectrum corresponds to the mean of three consecutive sweeps, automatically calculated by the PSV (9.2).

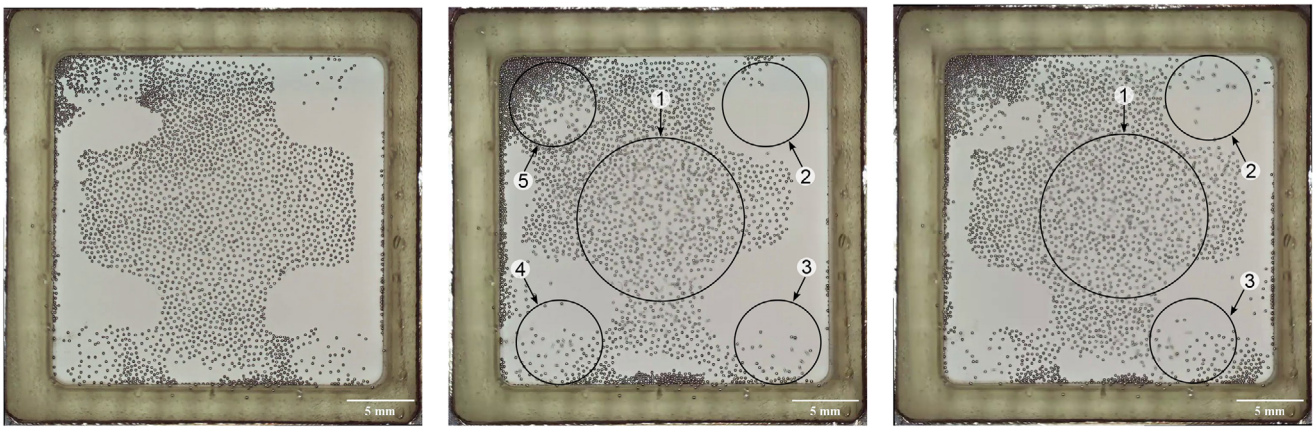

(a) (b) (c)

Figure 15. Distribution of metal alloy balls on a dry membrane during the particle manipulation experiments: a) initial distribution, b) distribution after 10 s of agitation in the 3500–3600 Hz interval, and c) distribution after another 10 s of agitation in the 6700–6800 Hz interval. The source videos are included in the video attachment.

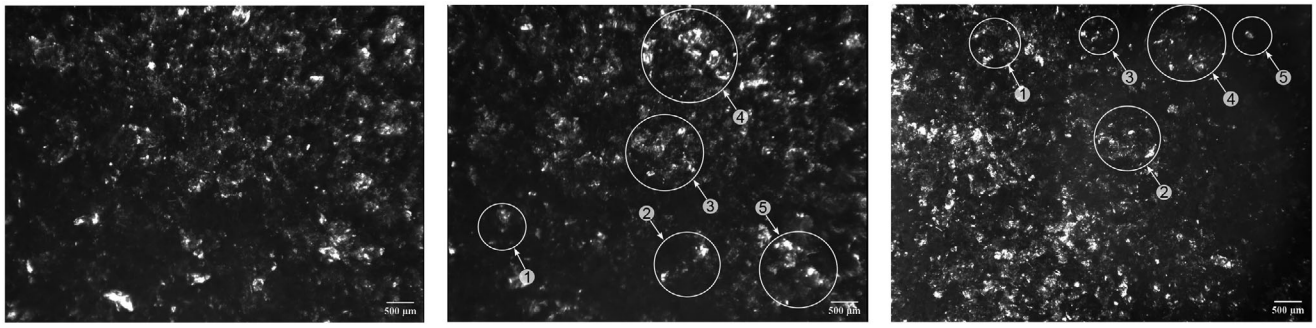

(a) (b) (c)

Figure 16. Visualization of particle manipulation with 1 wt% Iriodin suspension: a) initial state of the suspension, b) state after 10 s of agitation in the 3100–3200 Hz interval at 700 V_{pp}, and c) state after another 10 s of agitation in the 5400–5500 Hz interval at 700 V_{pp}. The source videos are included in the video attachment.

a number of resonant peaks above 2 kHz. Adding the metal alloy spheres shifted the first resonances to lower frequencies (684 Hz and vicinity of 1260 Hz) due to the added mass. The elevated magnitude and damping in the low-frequency range (+1 m s^{-2} Hz^{-1} slope below 684 Hz and suppressed peaks above 2 kHz) are likely due to the motion of metal spheres and collisions with the membrane. Adding water to the membrane (in addition to the metal spheres) further lowered the first resonant frequencies (200–800 Hz). It caused the average accelerations to plateau above 2 kHz (0 m s^{-2} Hz^{-1} slope) due to the increased mass. While a marginal increase is observable in magnitude and damping in the low-frequency range (+1 m s^{-2} Hz^{-1} slope below 80 Hz), the behaviour is closer to the free membrane as water reduces the mobility of the balls. Experiments with Iriodin suspension exhibit similar resonant frequencies and high-frequency behavior to those of metal spheres and water as a result of the similar load. Since the membrane is not visible through the suspension, these experiments directly measure the motion of the mobile Iriodin flakes in water, causing similar elevated magnitude and damping behavior in the low-frequency range (below ca. 500 Hz).

The behavior of the metal balls (dry) and Iriodin suspension on the agitated membrane was visualized by recording the surface under a microscope, as visualized in the video attachment (see Video S1, Supporting Information). Agitation was applied in the vicinity of 3512 Hz (plateau region after the corner frequencies of the fluid-loaded membranes) and 6733 Hz (highest accelerations for the membrane with metal alloy balls), as indicated in Figure 14. Sweep signals in the 3500–3600 Hz and 6700–6800 Hz intervals were applied at incrementally increasing voltages to better visualize particle dynamics on the membrane, before damaging the actuator. The reported results correspond to the 500 V amplitude, which is well above the previously identified 300 V threshold of the 25 µm thick EAP layer.

Figure 15 shows the membrane with randomly distributed metal alloy balls on the membrane surface prior excitation (Figure 15), after 10 s excitation in the 3500–3600 Hz interval (Figure 15) and 10 s of excitation in the 6700–6800 Hz interval (Figure 15). As shown in Figure 15, it was not possible to cover the membrane area directly opposite to the bottom electrode pattern due to the electrostatic repulsion of the particles. Agitation causes the particles to redistribute and vibrate on the membrane, observable as motion in the video and as motion blur in the still images (Figure 15). Regions with most particle motion are marked and numbered, including the center of the membrane (marked as 1) and the transducer areas (marked as 2-5). The membrane motion pattern corresponds to the distribution of nodes and anti-nodes in the excited vibration modes, with clear differences observed between the 3500–3600 Hz and 6700–6800 Hz ranges. However, the fidelity of particle motion in the video is insufficient to accurately identify the modal composition of the membrane motion. Metal alloy balls damp the high-frequency resonance peaks, preventing the formation of the distinct Chladni patterns of modal anti-nodes.[49]

Figure 16 illustrates the membrane with Iriodin suspension (1 wt% in deionized water), shown before (Figure 16) and after agitation at two distinct frequency ranges: around 3150 Hz (Figure 16) and 5450 Hz (Figure 16), chosen at the acceleration magnitude peaks of the LDV measurements (Figure 14). Sweep signals in the 3100–3200 Hz and 5400–5500 Hz intervals were incrementally increased in voltage and achieved reliable operation at up to 700 V (peak-to-peak) agitation. It is hypothesized that the Iriodin suspension improves heat dissipation that occurs due to the hysteresis in the P(VDF–TrFE–CTFE) active layer, improving the breakdown strength. Motion of the Iriodin particles are observable in the recordings due to the changing reflection pattern, whereas the still frames in Figure 16 are marked to indicate five regions with clear changes before and after the 10 s experiments.

3.4. Outlook

Mechanical agitation of filtration membranes through embedded actuation is therefore capable of mobilizing and redistributing particles on the filtration membrane and in its vicinity. This is a promising indication of its viability for developing active membranes that can prevent fouling or recover their functionality. Incorporating self-cleaning functionality increased membrane expenses by approximately 116% and 378% for the PVDF membrane PTFE membrane, respectively (excluding labor). However, scaling up production is expected to significantly reduce the material and reactant costs and diminish the equipment and labor costs. A significantly extended membrane lifetime has therefore a

good potential to enhance overall cost-effectiveness over the conventional membranes.

As this study focused on actuator integration and membrane dynamics, the ongoing research now advances towards practical implementation of the active filtration membrane concept, with emphasis on flux recovery and long-term fouling suppression. First, a significant redesign of the filtration module (see Figure 5) is required to form a closed system for filtration experiments (e.g., under controlled flow or pressure). The antifouling performance will then be quantified via flux recovery (before and after actuation) and fouling prevention (under constant actuation) experiments, using model foulant solutions. The actuator structure, geometry and placement will be optimized to maximize performance while minimizing the loss of effective filtration area. While no signs of delamination were observed in this study, the durability and failure modes of the active membrane (especially the adhesion between filtration membrane, electrodes and sealing layers) will be studied to assure structural integrity over long term operation.

4. Conclusion

This research proposed a novel active filtration membrane concept that combines polymeric filtration membranes with electroactive polymer actuators for embedded self-cleaning functionality. This approach allows to: 1) decouple membrane fabrication from actuation to activate already available membrane technologies; 2) introduce high-transduction EAPs directly to the vibration sites to improve agitation efficiency; and 3) electrically isolate the filtrate from the actuation voltages to ensure compatibility with real-life feed solutions.

P(VDF–TrFE–CTFE) actuators were patterned on PVDF and PTFE microporous filtration membranes to create actuation regions that stimulate out-of-plane vibrations. Dynamics and particle manipulation were studied and the effects of membrane material selection, actuator placement and active layer thickness were considered. Active membranes produced out-of-plane accelerations of up to 75 m s^{-2} (600 V, 4548 Hz) and local surface accelerations of up to 255 m s^{-2} (600 V, 6560 Hz). The effect of different loading conditions on membrane dynamics was measured using metal alloy balls (200 µm), water and Iriodin 153 Flash Pearl suspension (1 wt%). Experiment recordings visually confirmed the mobility and redistribution of the particles.

Therefore, for the first time, polymeric actuator have been embedded on porous polymeric filtration membranes and their electrodes have been electrically isolated from the fluids (feed and filtrate). Experiments both in air and aqueous environments confirmed that the active membranes are capable of mobilizing and redistributing particles on the filtration membrane and in its vicinity. Future work will further address the antifouling performance of the active membranes, viability of foulant removal from the membrane area, and optimization of actuator placement and morphology.

Supporting Information

Supporting Information is available from the Wiley Online Library or from the author.

Acknowledgements

The authors wish to acknowledge the faculty of Mechanical Engineering, Delft University of Technology, Netherlands, for funding this project as part of the cohesion grants. H.B. also acknowledge the Dutch organization for scientific research (NWO) for funding this work through the open competition grant in the domain of science (grant number OCENW.XS22.1.002).

Conflict of Interest

The authors declare no conflict of interest.

Data Availability Statement

The data that support the findings of this study are available from the corresponding author upon reasonable request.

Keywords

electro-active polymer (EAP) actuators, embedded actuation, laser Doppler vibrometer, microfiltration membranes, particle manipulation, resonance, spray printing

Received: August 5, 2025
Revised: September 30, 2025
Published online: November 14, 2025

[1] N. Shehata, D. Egirani, A. G. Olabi, A. Inayat, M. A. Abdelkareem, K. J. Chae, E. T. Sayed, *Chemosphere* **2023**, *320*.
[2] T. A. Tellaa, B. Festus, T. D. Olaoluwa, A. S. Oladapo, in *Smart Nanomaterials for Environmental Application* (Eds.: O. O. Ayeleru, A. O. Idris, S. Pandey), Elsevier, Cham **2024**, pp. 351–385, https://www.sciencedirect.com/science/article/pii/B9780443217944000302?via%3Dihub.
[3] A. Mojiri, M. J. Bashir, *Water* **2022**, *14*, 448.
[4] K. Saravanakumar, S. De Silva, S. S. Santosh, A. Sathiyaseelan, A. Ganeshalingam, M. Jamla, A. Sankaranarayanan, V. P. Veeraraghavan, D. MubarakAli, J. Lee, G. Thiripuranathar, M. H. Wang, *Chemosphere* **2022**, *307*.
[5] E. O. Ezugbe, S. Rathilal, *Membranes* **2020**, *10*, 89.
[6] H. Shemer, S. Wald, R. Semiat, *Membranes* **2023**, *13*, 612.
[7] M. Ehsani, H. Doan, A. Lohi, *Korean J. Chem. Eng.* **2021**, *38*, 1531.
[8] C. Li, X. Guo, X. Wang, S. Fan, Q. Zhou, H. Shao, W. Hu, C. Li, L. Tong, R. R. Kumar, J. Huang, *Electrochim. Acta* **2018**, *287*, 124.
[9] W. Guo, H. H. Ngo, J. Li, *Bioresour. Technol.* **2012**, *122*, 27.
[10] Y. J. Wang, C. X. Li, Y. Meng, Z. Y. Guo, S. Cui, X. Z. Fu, H. Q. Liu, W. Q. Xia, W. W. Li, *Water Res.* **2024**, *250*.
[11] X. Lu, L. Shen, Q. Zeng, J. Du, C. Chen, J. Teng, W. Yu, Y. Xu, H. Lin, *J. Membr. Sci.* **2024**, *692*.
[12] A. Kim, J. Hak Kim, R. Patel, *Bioresource Technol.* **2022**, *345*, 126501.
[13] X. Zhao, R. Zhang, Y. Liu, M. He, Y. Su, C. Gao, Z. Jiang, *J. Membrane Sci.* **2018**, *551*, 145.
[14] R. R. Choudhury, J. M. Gohil, S. Mohanty, S. K. Nayak, *J. Mater. Chem.* **2018**, *6*, 313.
[15] M. M. Motsa, B. B. Mamba, J. M. Thwala, A. R. Verliefde, *Desalination* **2017**, *402*, 62.
[16] A. Gul, J. Hruza, F. Yalcinkaya, *Polymers* **2021**, *13*, 846.
[17] Y. Zhao, F. Yang, H. Jiang, G. Gao, *Nat. Commun.* **2024**, *15*, 1.
[18] E. Pantuso, E. Ahmed, E. Fontananova, A. Brunetti, I. Tahir, D. P. Karothu, N. A. Alnaji, G. Dushaq, M. Rasras, P. Naumov, G. Di Profio, *Nat. Commun.* **2023**, *14*, 1.

[19] Y. P. Su, L. N. Sim, X. Li, H. G. Coster, T. H. Chong, *J. Membr. Sci.* **2021**, *620*.
[20] J. Gao, Z. Zhu, M. Qiu, X. Chen, Y. Fan, *Environ. Chem. Eng.* **2024**, *12*, 112105.
[21] H. Mao, W. Fan, H. Cao, X. Chen, M. Qiu, H. Verweij, Y. Fan, *Sep. Purif. Technol.* **2022**, *282*.
[22] L. Grilli, F. Casset, C. Bressy, H. Brisset, J. F. Briand, R. Barry-Martinet, M. Colin, *Actuators* **2022**, *11*, 2.
[23] H. Mao, M. Qiu, J. Bu, X. Chen, H. Verweij, Y. Fan, *ACS Applied Materials and Interfaces* **2018**, *10*, 18093.
[24] J. K. Krinks, M. Qiu, I. A. Mergos, L. K. Weavers, P. J. Mouser, H. Verweij, *J. Membr. Sci.* **2015**, *494*, 130.
[25] D. Chen, C. Pomalaza-Ráez, *Sep. Purif. Technol.* **2019**, *215*, 612.
[26] M. T. Darestani, H. G. Coster, T. C. Chilcott, *J. Membr. Sci.* **2013**, *435*, 226.
[27] H. F. M. Austria, R. P. Sardome, O. Setiawan, T. H. Huang, W. C. Lei, X. Y. Tian, C. C. Hu, K. R. Lee, J. Y. Lai, L. L. Tayo, A. R. Caparanga, W. S. Hung, *Sep. Purif. Technol.* **2024**, *346*.
[28] D. Kuscer, T. Rojac, D. Belavič, M. S. Zarnik, A. Bradeško, T. Kos, B. Malič, M. Boerrigter, D. M. Martin, M. Faccini, *J. Membr. Sci.* **2017**, *540*, 277.
[29] N. M. A. Omar, M. H. D. Othman, Z. S. Tai, M. Milad, M. N. M. Sokri, M. H. Puteh, *Appl. Cer. Technol.* **2023**, *20*, 3327.
[30] R. J. Santucci, J. R. Scully, *Proc. Natl. Acad. Sci. USA* **2020**, *117*, 23211.
[31] H. Lin, Y. Ding, *J. Polym. Sci.* **2020**, *58*, 2433.
[32] L. R. Devi, B. D. Naorem, A. Chowdhuri, H. B. Sharma, *J. Alloys Compd.* **2024**, *1004*.
[33] Y. Bar-Cohen, V. Cardoso, C. Ribeiro, S. Lanceros-Méndez, in *Advanced Piezoelectric Materials*, 2nd ed. (Eds.: K. Uchino), Woodhead Publishing, UK **2017**, pp. 319–352.
[34] X. Chen, X. Han, Q. D. Shen, *Adv. Electron. Mater.* **2017**, *3*, 1600460.
[35] V. Jaarsma, *MA thesis, Delft University of Technology* Netherlands **2023**, http://repository.tudelft.nl/.
[36] F. Ganet, M. Q. Le, J. F. Capsal, J. F. Gérard, S. Pruvost, J. Duchet-Rumeau, S. Livi, P. Lermusiaux, A. Millon, P. J. Cottinet, *Sens. Actuators, B* **2015**, *220*, 1120.
[37] TECHNICAL GUIDE PIEZOTECH ® RT-TS, Technical report, Piezotech by Arkema, **2020**, www.piezotech.eu.
[38] S. IJssel de Schepper, A. Hunt, *Addit. Manuf.* **2024**, *81*.
[39] Metalon-JR-700HV-TDS, Technical report, Novacentrix, **2020**, https://www.novacentrix.com/datasheet/Metalon-JR-700HV-TDS.pdf.
[40] T. A. Baaij, Challenge the future Department of Precision and Microsystems Engineering Designing, manufacturing and testing bimorph piezoelectric twisting actuators, **2024**, http://repository.tudelft.nl/.
[41] P. Neeteson, Challenge the future Department of Precision and Microsystems Engineering Designing. Fabricating a Soft Robotic Fish Using Polyvinylidene Fluoride-based Actuators, **2024**, http://repository.tudelft.nl/.
[42] PVDF, Technical report, **2025**, https://www.professionalplastics.com/professionalplastics/content/PVDF.pdf.
[43] (PTFE) Polytetrafluoroethylene Physical Properties Metric English Comments, Technical report, https://www.professionalplastics.com/professionalplastics/content/Teflon_PTFE.pdf.
[44] Y. Bar-cohen, in *19th AIAA Applied Aerodynamics Conference*, Fluid Dynamics and Co-located Conferences. American Institute of Aeronautics and Astronautics, Reston, VA **2001**, https://doi.org/10.2514/6.2001-1492.
[45] L. Meirovitch, *Fundamentals of Vibrations*, Waveland Press, Long Grove, IL **2010**.
[46] A. G. M. Neves, Eigenmodes and eigenfrequencies of vibrating elliptic membranes: a Klein oscillation theorem and numerical calculations, Technical report, **2009**.
[47] L. Courbin, A. Marchand, A. Vaziri, A. Ajdari, H. A. Stone, *Phys. Rev. Lett.* **2006**, *97*, 24.
[48] K. Kalinova, in *Resonance*, InTech, **2017**.
[49] G. Vuillermet, P. Y. Gires, F. Casset, C. Poulain, *Phys. Rev. Lett.* **2016**, *116*, 18.